water

MDPI

Article

Experimental Application of Sediment Flow Connectivity Index (SCI) in Flood Monitoring

Marina Zingaro [1,*], Alberto Refice [2], Annarita D'Addabbo [2], Renaud Hostache [3], Marco Chini [3] and Domenico Capolongo [1]

[1] Department of Earth and Geoenvironmental Sciences, University of Bari "Aldo Moro", 70125 Bari, Italy; domenico.capolongo@uniba.it
[2] Consiglio Nazionale delle Ricerche—Istituto per il Rilevamento Elettromagnetico dell'Ambiente (CNR—IREA), 70126 Bari, Italy; alberto.refice@cnr.it (A.R.); annarita.daddabbo@cnr.it (A.D.)
[3] Department of Environmental and Innovation (ERIN), Luxembourg Institute of Science and Technology (LIST), L-4422 Belvaux, Luxembourg; renaud.hostache@list.lu (R.H.); marco.chini@list.lu (M.C.)
* Correspondence: marina.zingaro@uniba.it

Received: 29 May 2020; Accepted: 24 June 2020; Published: 28 June 2020

Abstract: Sediment connectivity is considered a powerful geomorphic indicator for defining the most sensitive areas to geomorphological modifications in a fluvial catchment (hotspots). This encourages the development of methods and models for its assessment, to investigate the interrelation of the various phenomena that occur in a river basin (landslides, floods, etc.). This work explores the potential connection of the processes in flood dynamics, by focusing on induced flood hazard, in order to evaluate the applicability of sediment connectivity to flood monitoring. By applying the recently developed sediment flow connectivity index (SCI) computation method to the Severn River basin, in UK, recurrently affected by floods, we investigate the agreement between the hotspot areas (described by the index) and the areas recurrently flooded (as mapped by aerial photography, satellite imagery and hydrodynamic modelling). Qualitative and quantitative approaches are used for the analysis of past (March 2007 and January 2010) as well as predicted (with return periods of 200 and 500 years) flood events. The results show a good correspondence of areas of high sediment connectivity with flood occurrence. Moreover, the detection performance of the SCI is slightly better than that of a simple flow accumulation map, confirming the importance of the initial mapping of sediment availability and mobility. This experiment extends the direct applicability of the SCI from fluvial analysis to flood monitoring, thus opening interesting future scenarios.

Keywords: sediment connectivity; SCI index; SAR; flood monitoring; flood hazard

1. Introduction

Sediment connectivity represents an important geomorphic indicator to evaluate the erosion, transport and deposition processes over time in fluvial basins [1–3]. The visualization of sediment pathways contributes to the understanding of catchment dynamics by identifying the contiguity of landscape components (structural connectivity) and their interaction in geomorphic, hydrological and ecological systems (functional connectivity) [4–6]. It is therefore known that the estimation of the processes of supply, transfer and storage of the sediment on the surface and in the channels becomes relevant to explore geomorphological modifications and consequently to recognize the most sensitive areas in the catchment (hotspots) [7–9].

As this fundamental role of sediment connectivity is being recognized in the geomorphological analysis, during recent years the scientific community has shown a growing interest to investigate various aspects of connectivity (spatial and temporal scale, types of fluxes, degree of connection, impact on/from natural and anthropic dynamics, etc.) [10–15]. New approaches were developed in order to evaluate the sediment connectivity through indices that consider surface characteristics like topography and land cover [16,17], then integrated with a rainfall erosivity factor [18]. New methods quantify the hydrological and the material connectivity by exploring mobilization and transport processes in time (time scale, thresholds, excesses and losses, T-TEL method, [19]), also by using models for erosion and deposition rate estimation in order to investigate the interrelation with geomorphological and land use changes [20,21]. At the same time, new applications assess the role of sediment connectivity in river monitoring and management activities, taking into account the human impact in longitudinal, lateral and vertical connectivity in the catchment [22,23]. Indeed, besides the need to make the computation of sediment connectivity increasingly accurate and complete [4], it is just as useful to extend and improve its applicability, both in terms of spatial scale and in terms of geomorphic processes interrelation. In this perspective, the use of indicators as proxies for sediment yield quantification supports the modelling of sediment transport processes [24–26]. At the same time, the combined use of hydrologic, geomorphic, pedological and climatic parameters is explored together with their strong dependence from the spatial and temporal scale of observation [27–31]. As the morphological evolution is conditioned by, and in turn conditions, water and sediment displacement, it directly influences the dynamics of all events in the catchment (landslides, floods, etc.). Therefore, sediment connectivity can become a tool to evaluate and correlate the effects of the various geomorphic phenomena that affect the basin [32–38]. The analysis of flood events and the evaluation of flood hazard suggest that some geomorphological processes can influence flood dynamics, also having an impact on the induced flood hazard [9,37,39]. Figure 1 collects some schematic examples from recent literature, illustrating how flooding could occur in a river reach by the interaction between hydrological (discharge, water level, flow velocity, etc.) and geomorphological processes (erosion, deposition and transport of sediments). For instance: the increasing riverbed elevation due to sediment accumulation (aggradation) reduces channel capacity, causing floods (Figure 1a); instability of the banks due to the erosion process may cause bank collapse (Figure 1b), leading eventually to embankment failure and flooding; the rising riparian vegetation (Figure 1c) and the transport of wooden material in the channel (Figure 1d) increase flood risk by occluding channel sections. It is therefore evident that morphological modification processes can induce (and then are connected to) the flood processes. It could then be argued that river reaches affected by processes due to sediment connectivity may correspond to river reaches affected by flood processes. In this perspective, sediment connectivity estimation becomes crucial for flood monitoring analysis.

The present study focuses on the exploitation of sediment connectivity in flood hazard assessment, illustrating the application of the simplified approach of the sediment flow connectivity index (SCI) [40] to a river basin (Severn, UK). In spite of the local nature of the SCI as an indicator of sediment transfer, its mapping approach represents an efficient way to test sediment connectivity in relation with its above-mentioned role in influencing the flood phenomena that recurrently affect a river basin.

This work proposes an assessment of the link between high sediment connectivity and high flood occurrence along the channels, by comparing hotspot areas (high connectivity) and flooded regions. The comparison (both qualitative and quantitative) is aimed at assessing whether a direct or indirect connection of sediment fluxes continuity (i.e., a major sediment delivery) with a greater flood occurrence is identifiable. The underlying hypothesis in this study is that SCI can help detecting sediment paths, and that it can be applied in wide as well as small catchments, at both fine and coarse spatial resolutions. In fact, the recent availability of open datasets could extend such kinds of analyses to large catchments. For this aspect, this study follows the objective of leveraging the use of remote detection of connectivity in the catchment by combining different data sources [41–43].

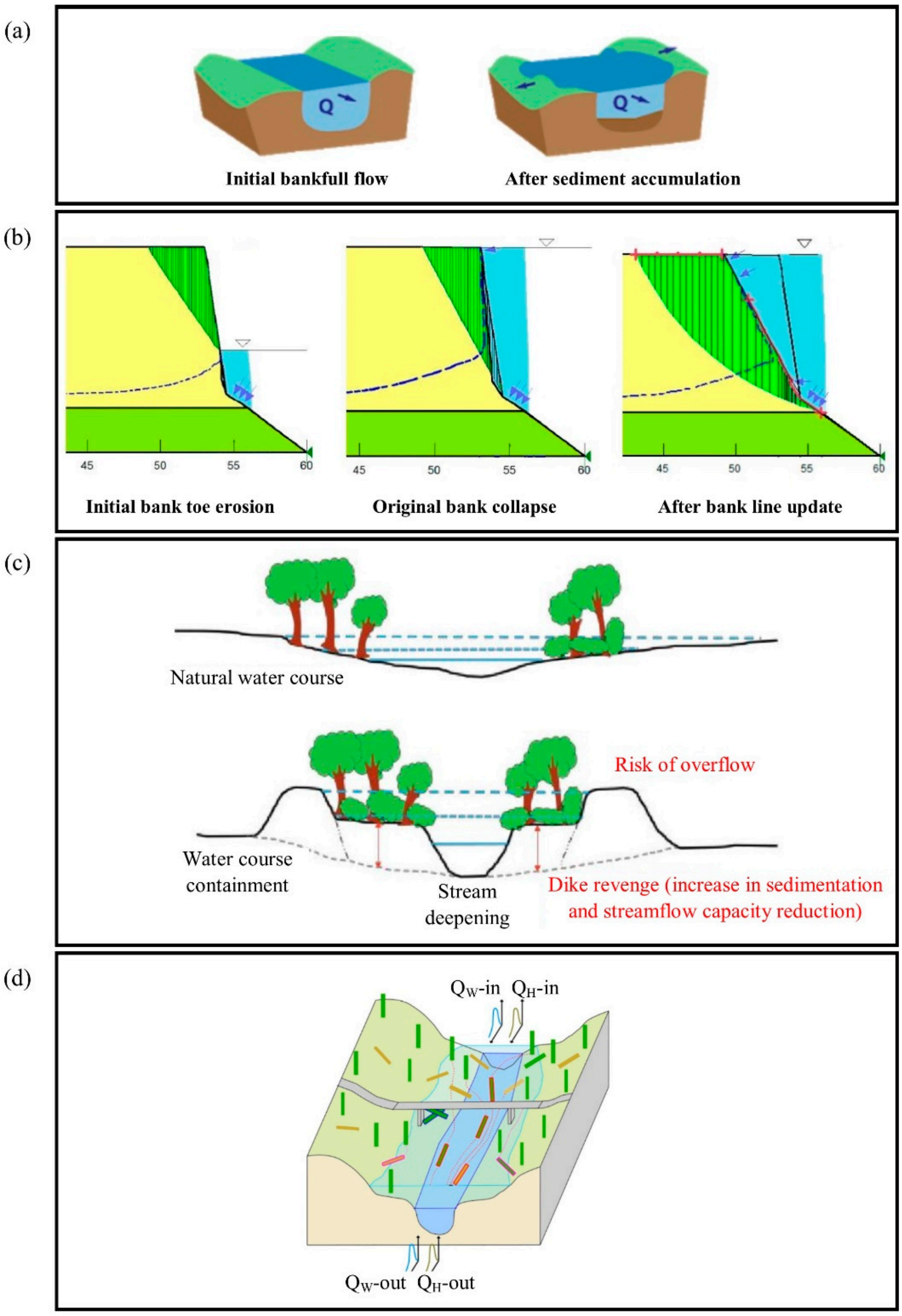

Figure 1. Some examples, taken from recent literature, of schematic representations of the interaction of deposition, erosion and transport processes with hydrological processes in induced flood phenomenon. (**a**) Sediment accumulation in the riverbed determines flooding. From "Modeling of HydroGeomorphic Hazards" project, University of Washington (http://notesbyshelby.blogspot.com/2018/12/quarter-1.html, last accessed on 26 June 2020). (**b**) Results from a numerical model simulation showing the erosion of a bank toe, affected by increasing river water level and a decreasing stability factor, causes bank collapse and riverbank state recovery after bank line update (from left to right of the box). From [44], Figure 14 (slightly modified). (**c**) Graphic illustrating schematically the role of the riparian vegetation in watercourses, and its effects on the speed and capacity of streamflow, leading to increased risk of overflow. From [45], Figure 10 (slightly adapted). (**d**) Schematic illustration of the transport of large wood debris and its accumulation (log-jam), creating local obstructions leading to flooding, especially at bridge locations. From [46], graphical abstract (slightly adapted).

2. Study Area

The geomorphologic features of the Severn River basin, in the central Wales and western regions of England, UK, characterized by the presence of a large floodplain, and the recurrence of floods with relative availability of data, make it suitable for the experimentation. This rather large catchment (21,590 km^2) includes three distinct geographic sectors, known respectively as Upper, Middle and Lower Severn [47] (Figure 2a). The Upper Severn flows from the Welsh Cambrian Mountains toward Ironbridge, where the fluvial erosion process has modelled a gorge. A sequence of ancient and recent terraces characterizes the Middle Severn with the alternating river action of erosion and deposition, which downstream from Worcester reflects also in the pattern of incision and aggradation with a series of buried channels. The Lower Severn in the Vale of Gloucester crosses the wide floodplain with a meandering course that, after receiving the main tributaries of the Teme and Avon rivers, flows in the Bristol Channel with a large estuary. The Lower Severn valley is covered by fluvial, glaciofluvial and glaciogenic deposits, and throughout the valley there are colluvial and local organic deposits. The lithological structure of the area is based on sandstone (Sherwood Sandstone Group), mudstone, quartz and quartzite, ironstone and limestone. Gravels are principally composed of Palaeozoic, Triassic and (mainly below the Avon confluence at Tewkesbury) Jurassic material from the local bedrock of the catchment, with an admixture of glacial material from the Anglian Wolston Formation and, in the younger terraces, a substantial admixture of "Irish Sea" glacial material from the Devensian Stockport Formation [48,49].

A marked gradient in topography and precipitation from west to east, and a range of geologic units and terrain types, underline the substantial spatial variability of the catchment. Furthermore, an extensive urbanization and land use variation make the surface more susceptible to changes, directly influencing sediment supply to the hydrographic network, that is particularly dense with important tributaries of the Severn, such as the Teme and Avon. Other channels, such as the Rivers Wye and Usk, are often not regarded as tributaries of the Severn since they flow into the estuary, but they are included in the Severn River basin district for flood management purposes. An area of the basin, located at the confluence of the Severn with the Teme and Avon rivers, was affected by flood events in the past, as investigated in several studies (see Section 3.3).

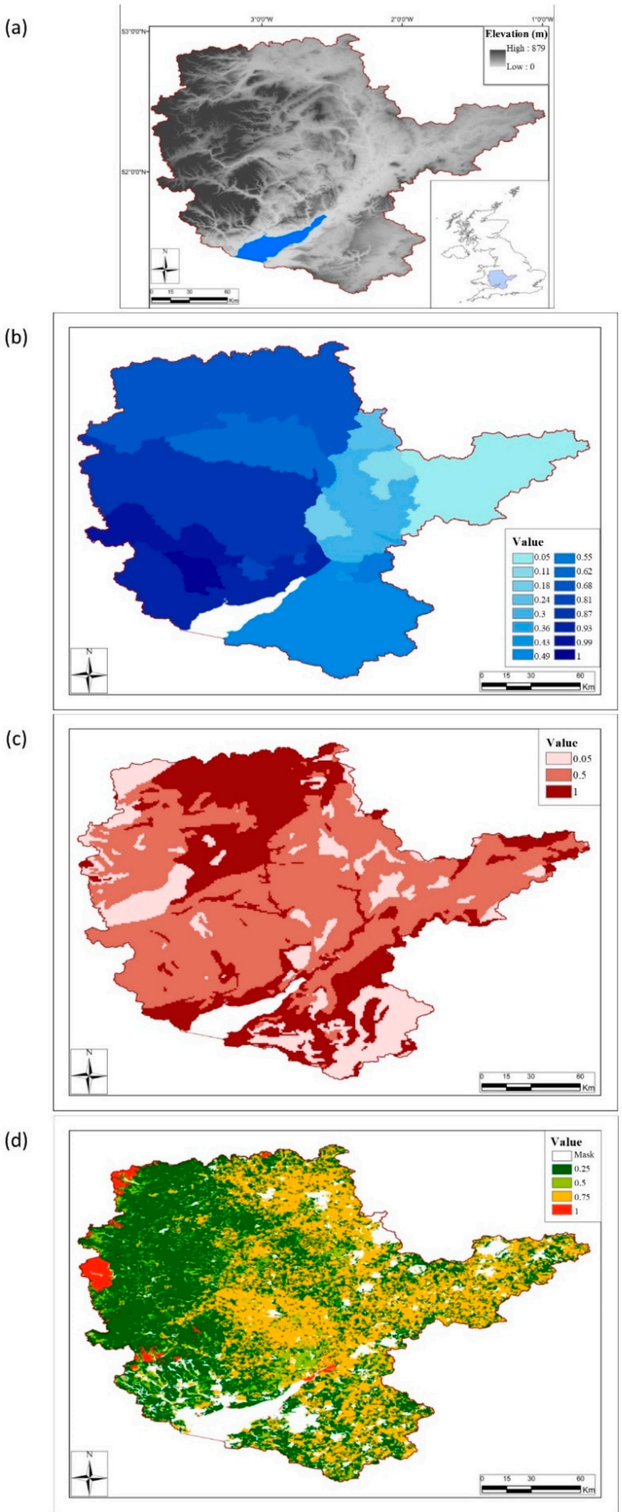

Figure 2. (**a**) Digital Elevation Model (DEM) of the Severn basin in southwestern England (SRTM30). (**b**) Rainfall data: sub-catchments of the Severn basin in the value classes (mean annual precipitation, from catchment daily rainfall (CDR) dataset). (**c**) Soil stability data: soil properties conditions in assigned value classes (from the harmonized world soil database (HWSD) and the British geological survey superficial deposit thickness model (BGS-SDTM)). (**d**) Land use data in associated value classes (from Corine land cover map (CLC), 2018). See text for the explanations.

3. Data and Methods

3.1. SCI Map Computation

The mapping approach developed by [40] is based on the concept of sediment connectivity as the potential connection among different areas of the fluvial basin through material transport (i.e., water and/or sediment flow). The method considers this (sediment) linkage an effect of two phenomena: the mobilization (erosion) of the sediment and its transfer along the channels to the outlet (target) both in lateral and longitudinal direction. As explained in [40], the mapping approach is divided in two steps: first, we estimate the sediment mobility considering the factors that control sediment erosion and mobilization, and secondly, we simulate sediment fluxes through slope-driven flow accumulation. In this way, we measure the connection of any raster cell with any other downstream cell by taking into account flow pathways. The approach tries to implement a functional aspect (flow accumulation) into a structural index (sediment mobility) in order to obtain a sediment flow connectivity index (SCI).

The first step consists of computing a sediment mobility index (SM), determined by two factors, SM_1 and SM_2, taking into account main annual rainfall, soil stability, and land use (SM_1) and surface characteristics (SM_2), respectively. The combination of these elements, which are well-known factors in connectivity estimation [16–18,50–52], allows modelling the conditions for sediment initial availability and movement on the surface.

SM is defined as:

$$\mathrm{SM} = \mathrm{SM}_1 \cdot \mathrm{SM}_2, \tag{1}$$

with:

$$\mathrm{SM}_1 = \frac{R}{SI}\, L, \tag{2}$$

$$\mathrm{SM}_2 = \frac{S}{Ru}, \tag{3}$$

where R is a rainfall index, SI is a soil stability index, L is a land use index, S is the slope and Ru is the surface ruggedness (i.e., a proxy of surface roughness, defined as the mean height difference between a central pixel and its surrounding cells in a 3×3 analysis window [40]). All the (dimensionless) indices are determined by categorizing the corresponding variables or terrain types in order of increasing potential to generate and mobilize the sediment, based on an a priori interpretation of the dynamics that affect the erosion phenomenon (rainfall amount for the climatic characterization, soil features for the drainage and runoff evaluation, land cover for surface behaviour). This procedure aims to standardize the method in order to apply it to any (medium-large) catchment. Obviously, this qualitative classification imposes a simplification of the complexity of surface processes and inevitably neglects some variables. In the following, we evaluate the incidence of this aspect on SM estimation, also considering the use of available open datasets to support or compensate for the lack of in situ data.

The second step is the computation of the final sediment flow connectivity index (SCI), obtained by using the SM map as a weighting raster within a classical flow accumulation algorithm F, in which SM values are propagated from higher to lower elevation pixels, thus simulating a "sediment contributing area" for each cell.

The procedure iteratively sums the weights (i.e., the SM values) of each cell to all its downslope connected cells, in order to determine the final output of accumulated sediment flow. In this way, a high cumulated value, due to a high sediment contributing area, indicates a high sediment flow, and vice versa. This assumes the flow accumulation as a proxy of material transport pathways, simplifying the sediment and water dynamics as a basic propagation in the steepest descendent direction. The final index is given by

$$\mathrm{SCI} = \log_{10} F(\mathrm{SM}) \tag{4}$$

A cell with a high value of SCI expresses a high accumulation of sediment from sediment-active cells (which contribute to sediment transfer), and vice versa.

In order to ease the SCI map applicability in fluvial monitoring, [40] proposed a lower spatial resolution version of the final map, by applying a mean filter through a rectangular window. This smoother map, here called a-SCI map, reduces the potential impact of high spatial frequency noise in the data. Also, it can be visualized through simple 3-color palettes as high, medium and low sediment connectivity, thus translating the specificity of the phenomenon into a simple graphic representation, understandable by a large number of end-users. In the present study, the a-SCI map constitutes the main tool to apply directly sediment connectivity to the flood context.

For further details and considerations regarding all methods here summarized, the reader is referred to [40].

3.2. SCI Map Data

All data considered for the SCI computation are extracted from open access datasets. The spatial resolution of all the considered maps is 30 m. This corresponds to the spatial resolution of the DEM (SRTM30, Shuttle Radar Topography Mission) used for extracting information from topographic data; data originally with a coarser resolution were resampled to 30 m.

Rainfall data refer to the mean annual precipitation (MAP) derived from catchment daily rainfall (CDR) long-term time series. CDR, provided from the National River Flow Archive (NRFA), are derived from CEH-GEAR data [53], a 1 km gridded rainfall dataset generated from the interpolation of observed rainfall of all rain gauges from the Met Office national database [54]. In the present study, MAP values related to the main sub-catchments that compose the basin were cumulated over the interval 1961–2015. This total rainfall over the basin was rescaled into index values from 0.05 to 1, as in [40] (see Table 1 and Figure 2b).

Table 1. Mean annual precipitation (MAP) in the Severn catchment classified in rainfall index values. The entire range (from maximum to minimum value of the temporal series) has been re-scaled from 0 to 1 (see text for details).

Rainfall MAP (mm per year)	Rainfall Index Values
667–668	0.05
669–719	0.11
720–772	0.18
773–825	0.24
826–878	0.3
879–931	0.36
932–984	0.43
985–1037	0.49
1038–1089	0.55
1090–1142	0.62
1143–1195	0.68
1196–1247	0.81
1248–1300	0.87
1301–1353	0.93
1354–1406	0.99
1407–1460	1

The soil stability index values were based on geotechnical soil properties classification. Soil units and relative attributes (permeability, bulk density and thickness) come from the Harmonized World Soil Database (HWSD, res. 1 km) and the British geological survey superficial deposit thickness model (BGS-SDTM, 1 km hex-grid). Realized by FAO and International Institute for Applied Systems Analysis (IIASA), HWSD combines existing regional and national updates of soil information worldwide and integrates them with the information contained within the 1:5,000,000 scale FAO-UNESCO Soil Map of the World (FAO, 1971–1981), (HWSD version 1.2, FAO/IIASA/ISRIC/ISS-CAS/JRC, 2012. Harmonized

World Soil Database—version 1.2. FAO, Rome, Italy and IIASA, Laxenburg, Austria). BGS-SDTM is a national scale dataset of superficial deposit thickness, produced by BGS to summarize thickness information via spatial statistics on the basis of a regular 1 km-sided hexagon grid distributed across the surface of Great Britain. For the present study, top-soil permeability (presence of an impermeable layer in the soil profile, in cm) and bulk density (kg/dm3) of soil units were extracted from HWSD, and the mean values of thickness (in m) were extracted from BGS-SDTM.

The soil properties were examined for a first classification (high, medium, low permeability etc., see Table 2), and then combined into a soil stability index with three classes, to which relative normalized values were assigned (see Table 3 and Figure 2c). The rationale of this classification is based on the interpretation of the role of soil properties in the stability dynamics. The selection of these soil properties is based on previous studies on soil stability dynamics in which permeability, layer thickness and plasticity were considered [40,55].

Table 2. Soil properties classification used for determining the soil stability conditions. The classes and the values of the properties (permeability, bulk density and thickness) are divided in categories (See text for details). LP = low permeability. MP = medium permeability. HP = high permeability. LH = low bulk density. HB = high bulk density. LT = low thickness. MT = medium thickness. HT = high thickness.

Soil Properties	Soil Properties Classes
Permeability classes	
Impermeable within 40 cm	LP
Permeable between 40 and 150 cm	MP
Permeable within 150 cm	HP
Bulk density values	
<1.4 kg/dm^3	LB
≥1.4 kg/dm^3	HB
Thickness classes	
≤1 m	LT
1–3 m	MT
≥3 m	HT

Table 3. Soil properties conditions classified in soil stability values (see text for details and previous caption for the abbreviations).

Soil Properties Conditions	Soil Stability Index Values
LP and HB or LT	0.05
MP and HB or MT	0.50
HP and LB or HT	1

In particular, the permeability is considered in association with the bulk density in order to evaluate the drainage and runoff capacity of the soil surface. The thickness is considered to evaluate the layer saturation.

The land cover index values were derived from the Corine land cover map (CLC) (version 2018, res. 100 m). As explained in [40], high values were assigned to classes that can favour sediment detachment (e.g., bare or poorly covered soil, arable land, cropland), lower values were attributed to land cover classes that were considered obstacles to sediment detachment (e.g., covered soil, pastures, grasslands). Urban areas were masked out assigning the 0 value. The classification is reported in Table 4 and Figure 2d.

Table 4. Land cover classes and index values associated with sediment mobility (see text for details).

Land Cover Classes	Land Cover Index Values
Urban areas	0
Grassland, pastures, shrubs, moorland	0.25
Woods, forests	0.50
Arable fields, croplands	0.75
Bare soils, wetlands	1

The slope (*S*) and ruggedness (*Ru*) raster maps used for SM_2 (see Section 3.1) are derived from the above-mentioned SRTM DEM. For the ruggedness computation, the TRI (terrain ruggedness index, [56]) was calculated by applying a tool implemented in the "gdaldem" module of the GDAL/OGR Geospatial Data Abstraction software Library (Open Source Geospatial Foundation, https://gdal.org). Since slope and ruggedness express the topographic variability in the catchment as local surface gradient and local surface height variation respectively, the SM_2 index has high values on the steep and/or regular surfaces, and low values on the flat and/or irregular surface. ArcMap™ (ESRI, www.esri.com) and QGIS® (Geographic Information System. Open Source Geospatial Foundation Project, http://qgis.org) software were used in the various steps of the procedure.

3.3. Flood Maps

We use flood maps derived from aerial photography, Synthetic Aperture Radar (SAR) images, and simulations, using visual interpretation, automatic floodwater mapping algorithm and hydrodynamic modelling, respectively. All data derive from previous and still ongoing research conducted on the Severn River catchment, in a specific test area at the confluence of the main river with the Teme and Avon tributaries (see Section 2), which have been recurrently flooded in recent years [57–62].

The photointerpretation was applied to aerial photos acquired on 24 July 2007, and consisted in visually mapping flooded areas [62]. Furthermore, aerial imagery of 31 July 2007 (available from Centre of Environmental Data Analysis archive website, https://catalogue.ceda.ac.uk/uuid/f73a1ed90ca550c350f587d43a5e20aa) were used for a visual comparison.

The Giustarini et al. algorithm [60] considers the pixel backscatter distribution in order to estimate a flood probability, providing probabilistic flood maps (PFMs), based on Bayesian inference, in which each pixel expresses the probability of being flooded (a value between 0 and 1), given its measured backscatter value. This approach quantifies the uncertainty associated with SAR-based flood extent maps. For a more detailed explanation of the procedure, refer to [60]. PFMs are here transformed into binary maps (flooded/not flooded), by selecting the 0.5 probability value as threshold.

Other flood binary maps derived from model simulations water depth maps are used, in order to consider additional flood events and corresponding water extents (i.e., flooded areas). Maps of predicted flood events with return period (RP) of 200 and 500 years, available for the test area, are obtained by adopting a consolidated methodology that involves hydrological analysis and hydrodynamic modelling [63,64]. The procedure includes (1) a statistical analysis of the long time series of hydrometric data (daily discharge) to derive the non-exceedance probability for predefined scenarios, and (2) LISFLOOD-FP model simulations to predict flood extent maps. Long-term time series of daily discharge acquired in seven gauging stations were processed. In order to obtain binary maps, a minimum water depth value of 10 cm was set as the threshold for each pixel.

All the flood maps were obtained originally with a coarser resolution of 75 m (for model set up see [63,64]) and were resampled to a spatial resolution of 30 m in order to apply the comparison with the a-SCI map.

3.4. SCI and Flood Maps Comparison

In order to compare SCI values with flood occurrence, qualitative and quantitative methods are applied.

The qualitative method is based on the visual analysis of the spatial coincidence of high sediment connectivity areas with flooded areas. The overlap of the observed flood water extent and the a-SCI map is considered for the events of 24 July 2007, and of 31 July 2007. For the other flood events, water extents derived from SAR images are used.

A second method is based on the quantitative analysis of the distribution of SCI values in flooded areas for selected flood events, both observed and predicted, to consider an increasing water extent. Firstly, histograms of SCI values over flooded and non-flooded areas are computed for each selected event in a smaller region of the test area. In this case the flooded area is composed by the pixels labelled as water on the extent maps previously described, while a buffer zone of 3000 m around the fluvial axis on both riversides, with the exclusion of the flooded areas, defines the non-flooded area. This test aims to evaluate the correspondence of higher SCI values with flooded areas, and vice versa. Secondly, receiver operating characteristic (ROC) curves are computed for each selected event, by using the flood map pixels as the "true" class and the a-SCI map as classified one, to identify false positive (fall-out) and true positive (sensitivity) rates. As a benchmark, ROC curves are also computed using a flow accumulation (FA) map as the classifier for each selected event. This test is finalized to compare the classification capacity of the SCI with respect to the role of sediment mobility—included in the SCI index and not included in FA—in flooded/non-flooded area classification. Classical FA algorithms start from unit values of flow on every pixel and propagate them downslope. Within the SCI definition, FA is used with an initial weighting of pixel values given by the SM map. Therefore, a comparison of the SCI map with a FA map (obtained with unit initial weights) allows quantifying the effect of the SM on the performance of the SCI, in this case as a flood indicator. The area under the curve (AUC) is the metric employed to evaluate the performance of the two classifiers.

4. Results

4.1. SM, SCI and a-SCI Maps

Figure 3 shows the maps obtained from Equation (1) and Equation (4) with red boxes highlighting some areas of the catchment. In the SM map (Figure 3a), computed from Equations (1)–(3), most of the catchment is characterized by a medium-high mobility (orange cells). While the areas with a greater sediment mobility (red cells) are distributed along the Upper, Middle and Lower Severn regions, the areas with a lower sediment mobility (blue cells) are mostly located in the eastern part of the catchment. This sediment mobility pattern is justified by the lower rainfall rate and the higher soil stability of the eastern basin compared to the greater rainfall rate, and the thinner and more permeable and compact soils of the high mobility areas. In some of the latter ones, a larger slope and ruggedness of the surface, as well as the presence of bare and arable soils, contribute to increase the mobility of the sediment (Upper-Middle Severn areas).

In the SCI map (Figure 3b), having values ranging between −4 (very low) and 8 (very high), the channels are identified by large values that show a spatial variation in relation with the longitudinal continuity of sediment and water flows (detail box). In the wider central part of the catchment, the SCI is high only along the main channels and in correspondence of the few red areas that can be considered as local sediment sources from which the hydrographic network receives sediment contribution. Moreover, dark green areas (very low SCI values), small but present throughout the whole basin, represent disconnected areas, in which the supply and the mobilization of sediment is likely very low or totally absent. The SCI map confirms the wide spatial variability of the Severn catchment, in which the variety of the sediment dynamics is distinguishable not only between different regions of the main river (i.e., Upper, Middle and Lower Severn), but also at a less extensive scale, with consequently smaller areas of observation (sub-catchments scale).

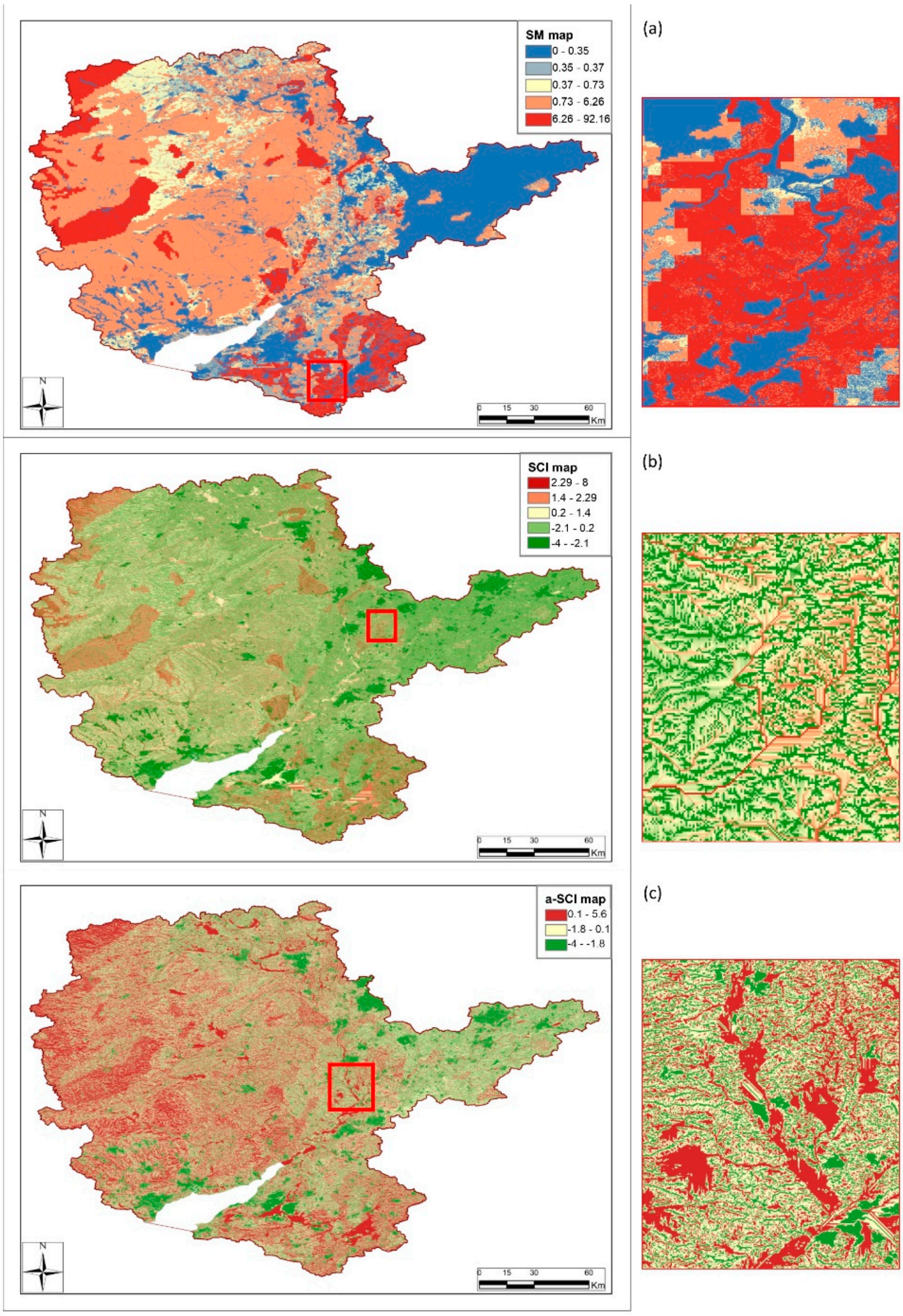

Figure 3. (**a**) Sediment mobility (SM) map (obtained from Equations (1)–(3)); (**b**) sediment flow connectivity index (SCI) map, and (**c**) a-SCI map of the Severn catchment. The detail maps on the right of each map correspond to the respective red boxes on the maps on the left, highlighting different areas of the catchment chosen to better illustrate the small scale characteristics of each index.

Figure 3c shows the a-SCI map, which better emphasizes the areas with high, medium and low sediment connectivity [40]. Here a 3 × 3 sliding window is used in the mean filter (see Section 3.1). In this smoother map, the areas with similar SCI values are more visible and the hot spot areas (red) are more easily identifiable. In the detail box on the right of the figure, the high sediment connectivity along the channels is well shown, by defining the border of the contiguous area with lower sediment connectivity (yellow and green).

4.2. SCI Comparison with Flood Occurrence

As a first comparison, water extents relative to the event that occurred on July 2007 were considered, by using event aerial photography acquired just after the event (see Section 3.4). As visible on the left of Figure 4, the flood water extent (blue-bordered areas) fairly well covers the areas with higher connectivity on the a-SCI map (red areas). Details of the areas along the main channels observed by aerial imagery (on the right of Figure 4) show that open water areas mostly correspond to high a-SCI areas (red box), while non-flooded areas coincide fairly well with low a-SCI areas (yellow box).

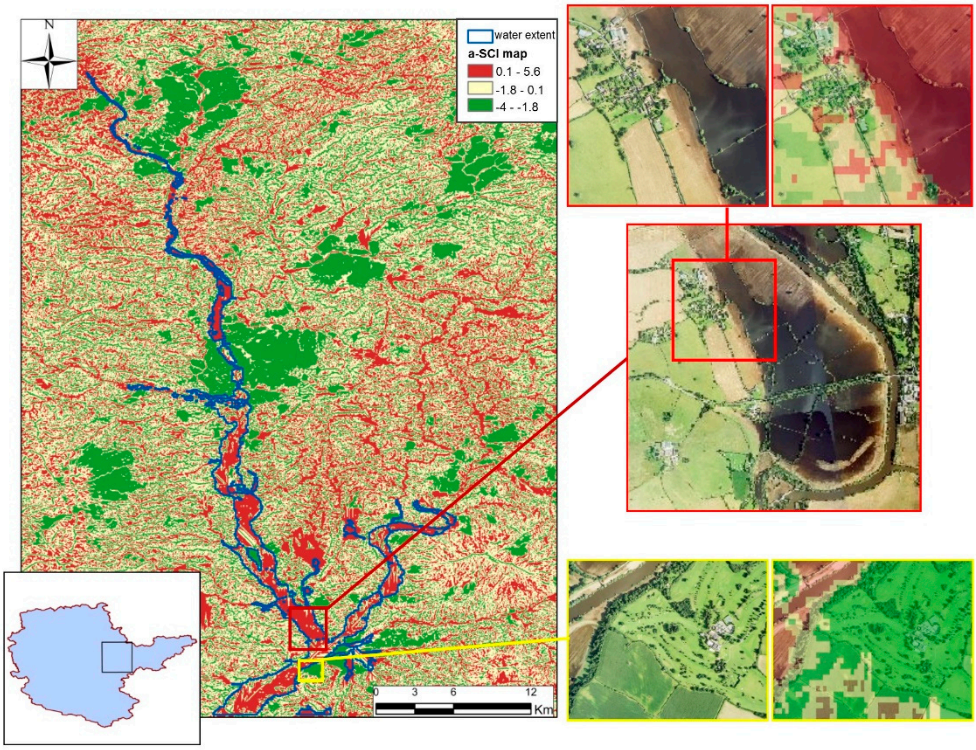

Figure 4. Visual validation of results on a sub-area of the Severn catchment (location map at the bottom-left). **Left:** a-SCI map with overlaid water extent borders (blue line) relative to the flood event that occurred on July 2007. **Right:** detailed comparison with aerial photography (res. 1 m, 31 July 2007) showing flooded areas (top, red box) corresponding to high sediment connectivity areas (in red) and non-flooded areas (bottom, yellow box) corresponding to low sediment connectivity areas (in green).

In a second comparison, the eleven flood maps from past events, obtained as described in Section 3.3, were considered (Figure 5).

A visual analysis shows a generally good correspondence of water extents relative to each event with the high connectivity areas, as the latter mostly fall within the border line of the flood regions (see flood occurrence map in Figure 5a). Each of the events that occurred between March 2007 and January 2010 can be seen to affect roughly the same areas, with an obvious variation of the water extent according to the relative magnitude. For this reason, the observed minimum, medium and maximum water extent were determined over a sub-area of the entire catchment, in order to focus the analysis (Figure 5b): the three regions (Figure 5c–e) fall quite well within the red area of the a-SCI map. Furthermore, the maximum water extent fits almost completely the boundary of the high connectivity zone.

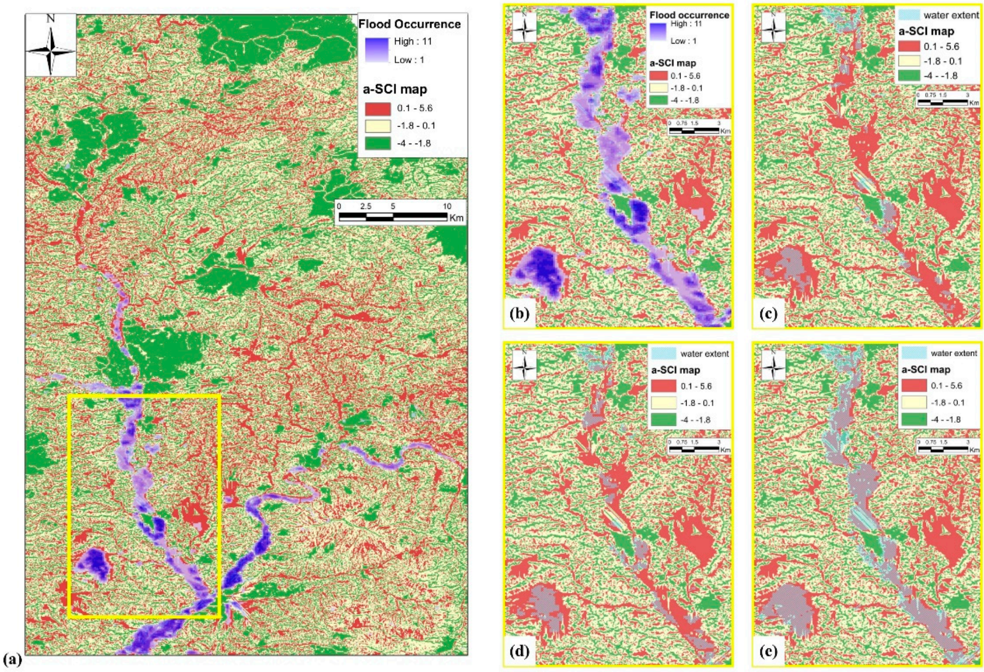

Figure 5. (**a**) a-SCI map and flood occurrence map relative to the 11 flood events considered (different blue gradient regions). (**b**–**e**) Yellow box in (**a**) shows (**b**) a detailed region with the selected (**c**) minimum, (**d**) medium, and (**e**) maximum water extent for the 11 events with the a-SCI map in background.

A quantitative analysis was then carried out by computing histograms related to flooded areas and non-flooded areas (Figure 6) for selected events (see Section 3.4). For the events for which remote sensing observations were available (shown in Figure 6a–c ordered in increasing intensity), a higher frequency of high a-SCI values demonstrates that the higher connectivity zone (a-SCI values between 0.1 and 5.6, as seen in the legend of Figure 4) almost totally covers the flood region. Conversely, a higher frequency of lower a-SCI values and a wider distribution of the samples characterize the non-flooded region, that corresponds to a medium-low connectivity area. For the two predicted events (RP 200, 500 years), the histograms show a similar behaviour (Figure 6d,e).

Figure 7 shows ROC curves relative to the a-SCI map and the flow accumulation (FA) map, obtained as explained in Section 3.4, for the same sequence of the events. The curve trends and the areas under the curve (AUCs) indicate two elements. First, the performance of the a-SCI map is better than that of the FA map for all examined samples (for all water extents). Second, the more frequent the event (and thus the smaller the water extent), the higher the capacity of the a-SCI index to recognize flooded areas as high-connectivity areas (AUCs of the blue ROC curves, from bottom to top of Figure 7). The efficiency of the FA maps in identifying flooded areas as high flow accumulation areas also improves similarly (AUCs of the red ROC curves).

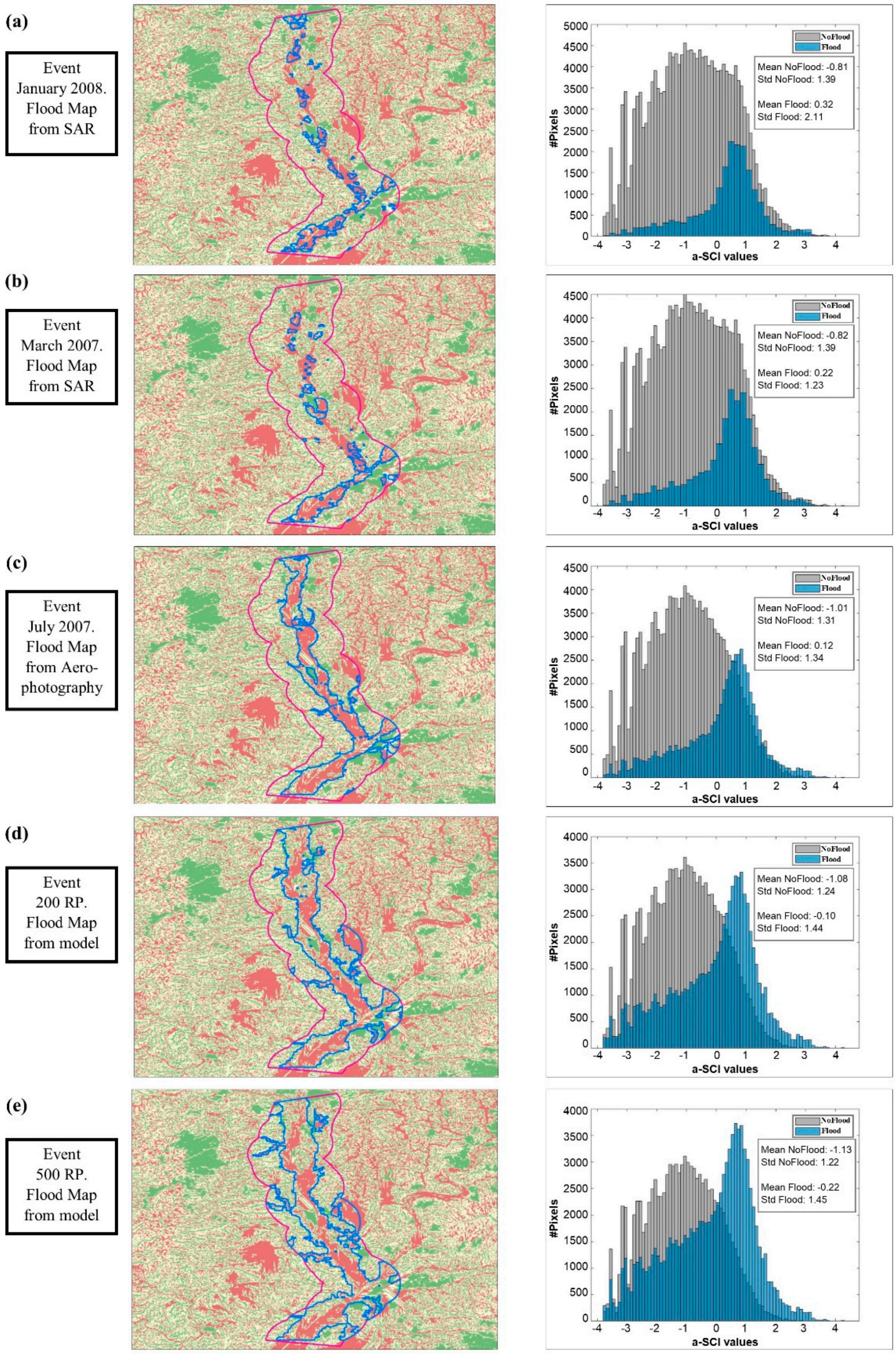

Figure 6. Histograms of a-SCI distributions for flooded and non-flooded areas, computed on a smaller area of the test site. Blue-bordered region: flooded area. Fuchsia-bordered region: buffer of 3000 m around the river course. (**a**–**e**) Flood and no flood areas in the considered flood events, observed (**a**–**c**) and predicted (**d**,**e**), ordered in increasing magnitude (maps on the left) and relative histograms (in blue and grey bins respectively, on the right).

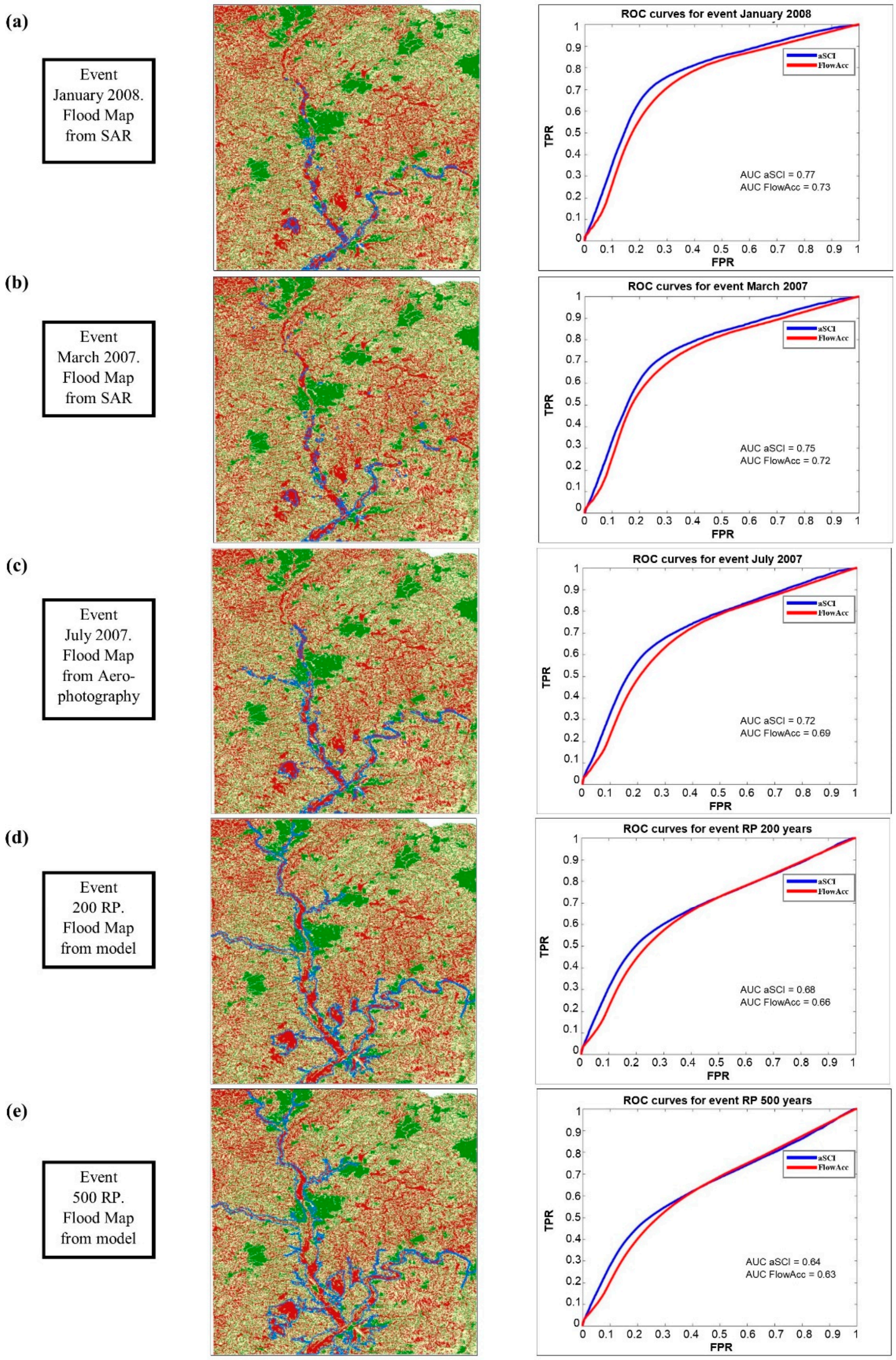

Figure 7. Receiver operating characteristic (ROC) curves and relative areas under the curve (AUCs) of a-SCI and flow accumulation (FA) maps performance in test area. (**a**–**c**) Flooded area (blue-bordered region, on the left) during observed flood events and corresponding ROC curves of a-SCI and FA maps (blue and red curves respectively, on the right). (**d**,**e**) Flooded area (blue-bordered region, on the left) in predicted flood events and corresponding ROC curves of a-SCI and FA maps (blue and red curves respectively, on the right).

5. Discussion

Although derived from low spatial resolution data (see Section 3), the SCI and a-SCI maps indicate that the upscaling and standardization of the weighting procedure does not significantly affect their application efficiency. Starting from the assumption that the appropriate spatial resolution in any mapping exercise strongly depends on the characteristics of the data and the objective of the study [28,43], the present experiment tells us that the assessment of sediment connectivity through the SCI is possible even at rather coarse resolution (30 m pixel size) in a rather large catchment such as the Severn basin.

The a-SCI map allows assessing the agreement between sediment connectivity and flood occurrence. Our results suggest that the channels and the areas along the channels that receive a higher contribution of water and sediment (due to their intense linkage with the sources and the paths of sediment flow) represent areas most active in the morphologic dynamics and, consequently, most sensitive to flood occurrence. This aspect makes the a-SCI map directly applicable in fluvial monitoring (as already proposed in [40]) and, at the same time, suitable for flood hazard monitoring. The a-SCI map identifies with a good precision the maximum possible water extent for events up to a relatively large return period (500 years), marked by the transition from the high connectivity zone (red in Figure 4) to the medium and low connectivity zone (yellow and green). If this is true, the high connectivity zone along the river (the Severn, in this case) could be considered the "sensitive" zone within which floods tend to occur. This result seems to be confirmed by the overlap of all eleven considered flood maps with the a-SCI map (Figure 5). Indeed, for the period considered (March 2007–January 2010), the flooded areas along the river are characterized by high sediment connectivity. In addition, the maximum extension reached by water during the flood phenomenon can be identified using the limit of the high connectivity zone. We argue that a more important sediment delivery in a river reach appears to be connected to flooding, either as a cause or an effect. Another element seems to confirm this observation: the green areas (low sediment connectivity), contiguous to the red areas, and thus to the flooded areas (see Figure 5), are not affected by any of the considered flood events. Moreover, the SCI tends to have higher values in the flood areas, as shown in Figure 6. However, this trend reduces as water extent increases (from Figure 6a to Figure 6e) covering therefore areas only flooded during high-magnitude, extreme events. The ROC curves confirm this scenario, showing a better trend for events of lower magnitude (blue curves in Figure 7). Another aspect that characterizes the final step of SCI index computation, i.e., the flow accumulation algorithm, could influence this result (see Section 3.1). Flow accumulation (FA) is often considered as a (simplistic) proxy of water pathways in a catchment, providing areas of accumulated flow in the valley bottom. The better performance of the SCI map with respect to the FA map performance (red curves in Figure 7) tells us that the sediment mobility taken into account by the SCI index contributes to improve the identification of high flood occurrence areas. Obviously, this better performance cannot completely describe the complex interrelation of the fluvial processes with the flood dynamics, including all the linkages between causes and effects of an extreme event. In other words, it cannot be excluded that high sediment connectivity does not always correspond to high flood occurrence, and vice versa. However, the better performance of the SCI index compared to the FA algorithm suggests that the sediment mobility helps considering other fundamental factors in flood susceptibility along the reaches. In fact, morphological and hydraulic reach conditions, determined by the fluvial processes and partly described by the SCI index, strongly influence the flood susceptibility of the reach. It is thus plausible that areas along the channels with high sediment connectivity (i.e., hotspot areas) correspond to flood prone areas, because the most active river reaches in water and sediment transport are presumably more susceptible to deliver sediment from the sources, representing remarkably imbalanced reaches. This means that the sediment transport between connected areas (sources and sinks) is intense and cannot be totally accommodated by the channels, producing changes in the fluvial dynamics, and consequently in the morphology of the surface [9].

In fact, modifications in the morphologic structure of the catchment generally affect the alluvial dynamics, because the areas where the flood propagates changes, influencing flow velocity and therefore the forces acting on sediment and water [65,66].

At the same time, the morphological variations of the channel sections directly affect the evolution of an inundation by obstructing or favouring the overflow and the water extent along that (modified) reach [37,39]. Indeed, as shown in Section 1, geomorphic features, such as banks erodibility, section variability (channel narrowing and aggradation), vegetation growth and/or accumulation of large wood, are considered in the evaluation of flood event effects (and causes), because they can represent natural barriers and/or impediment to the flow in the channel [38,67–71].

Finally, this experiment highlights the need to analyze in an integrated way the alluvial dynamics in a catchment, by exploiting information from different data sources. The possibility to recognize the hotspot areas (most morphologically dynamic and most frequently flooded areas) represents one additional tool in river phenomena investigation. Obviously, this dynamics agreement (sediment connectivity and flood occurrence) can be assumed reliable on the areas along the main channels of the catchment. This study shows that a-SCI map constitutes a valuable tool in flood monitoring and hazard assessment.

6. Conclusions

The sediment connectivity index (SCI) has been used to investigate the connection between basin processes in flood dynamics, in order to test its potential applicability in flood prone areas mapping and monitoring. The Severn River basin, UK, has been used as a test site because of its geomorphologic (large floodplain) and climatic (marked gradient of precipitation) characteristics and its frequent floodings, as well as the good data availability. The same procedure as in [40] has been used for the processing of the data, which has been extracted from open datasets. The lower spatial resolution version of the obtained SCI map, namely the a-SCI map, has been compared to flood maps of observed and predicted events (using respectively aerial and satellite imagery, and hydrodynamic modelling) in order to evaluate the correlation between the SCI-derived information and the flood occurrence along the rivers in the test area (at the confluence of the Severn with Teme and Avon tributaries). The results, obtained by visual interpretation and quantitative analysis, show a good correspondence between high sediment connectivity areas and high flood occurrence areas. This experiment therefore suggests that SCI is of high value in flood hazard analysis and monitoring.

More generally, the present work illustrates the contribution of an integrated analysis in the exploration of the phenomena that affect river catchment. Furthermore, data combination allows exploiting advantages of different sources of information (remote sensing, hydrodynamic modelling, geomorphometry) in river processes investigation.

Another element to mention is that the SCI can be computed by using open datasets, available on most (large) catchments, with the great advantage to obtain a description of sediment connectivity also in basins with limited in situ data. On the other hand, the typically coarse resolution of these dataset tends to underestimate the complexity of the surface by reducing the accuracy of the computation, also affecting the correspondence between the SCI and the flood occurrence. Future studies could decrease this uncertainty, by improving the computation methods and by exploiting increasingly more accurate open source data.

The complexity of the context that the work explores (interrelation of processes, integrated application, new research fields) partially limits the assessment procedure, as evaluation datasets are very difficult if not impossible to observe in the field.

Author Contributions: Conceptualization, M.Z., D.C. and A.R.; methodology, M.Z., D.C. and A.R.; validation, M.Z., A.R., A.D. and D.C.; formal analysis, A.R., A.D., D.C. and R.H.; investigation, M.Z., A.R. and D.C.; resources, M.Z. and D.C.; data curation, M.Z., R.H. and M.C.; writing—original draft preparation, M.Z., A.R., D.C., R.H., M.C. and A.D.; writing—review and editing, M.Z., A.R., D.C., R.H. and M.C.; visualization, M.Z., A.R., D.C., R.H. and M.C.; supervision, M.Z. and D.C.; project administration, M.Z., A.R. and D.C.; funding acquisition, M.Z., D.C., R.H. and M.C. All authors have read and agreed to the published version of the manuscript.

Funding: This research was supported by the contribution of the PON FSEFESR Research and Innovation 2014–2020 for Innovative and Industrial PhDs, from which M.Z. was funded. The contribution of R.H. and M.C. was supported by the National Research Fund of Luxembourg through the CASCADE Project under Grant C17/SR/11682050. The contribution of A.R. and A.D. was supported by the Italian Ministry of Education, University and Research, in the framework of the project OT4CLIMA, D.D. 2261–6.9.2018, PON R&I 2014–2020.

Acknowledgments: The authors thank Patrick Matgen for his valuable comments.

Conflicts of Interest: The authors declare no conflict of interest.

References

1. Caine, N.; Swanson, F.J. Geomorphic Coupling of Hillslope and Channel Systems in Two Small Mountain Basins. *Z. Geo-Morphol.* **1989**, *33*, 189–203.
2. Hooke, J. Coarse Sediment Connectivity in River Channel Systems: A Conceptual Framework and Methodology. *Geomorphology* **2003**, *56*, 79–94. [CrossRef]
3. Wohl, E. Connectivity in Rivers. *Prog. Phys. Geogr. Earth Environ.* **2017**, *41*, 345–362. [CrossRef]
4. Heckmann, T.; Cavalli, M.; Cerdan, O.; Foerster, S.; Javaux, M.; Lode, E.; Smetanová, A.; Vericat, D.; Brardinoni, F. Indices of Sediment Connectivity: Opportunities, Challenges and Limitations. *Earth-Sci. Rev.* **2018**, *187*, 77–108. [CrossRef]
5. Turnbull, L.; Wainwright, J.; Brazier, R.E. A Conceptual Framework for Understanding Semi-Arid Land Degradation: Ecohydrological Interactions across Multiple-Space and Time Scales. *Ecohydrology* **2008**, *1*, 23–34. [CrossRef]
6. Wainwright, J.; Turnbull, L.; Ibrahim, T.G.; Lexartza-Artza, I.; Thornton, S.F.; Brazier, R.E. Linking Environmental Régimes, Space and Time: Interpretations of Structural and Functional Connectivity. *Geomorphology* **2011**, *126*, 387–404. [CrossRef]
7. Bracken, L.J.; Turnbull, L.; Wainwright, J.; Bogaart, P. Sediment Connectivity: A Framework for Understanding Sediment Transfer at Multiple Scales. *Earth Surf. Process. Landf.* **2015**, *40*, 177–188. [CrossRef]
8. Vergari, F.; Della Seta, M.; Del Monte, M.; Barbieri, M. Badlands Denudation "Hot Spots": The Role of Parent Material Properties on Geomorphic Processes in 20-Years Monitored Sites of Southern Tuscany (Italy). *CATENA* **2013**, *106*, 31–41. [CrossRef]
9. Wohl, E.E. *Rivers in the Landscape: Science and Managment*; John Wiley & Sons Inc.: Hoboken, NJ, USA, 2014.
10. Brierley, G.; Fryirs, K.; Jain, V. Landscape Connectivity: The Geographic Basis of Geomorphic Applications. *Area* **2006**, *38*, 165–174. [CrossRef]
11. Doyle, M.W.; Ensign, S.H. Alternative Reference Frames in River System Science. *BioScience* **2009**, *59*, 499–510. [CrossRef]
12. Faulkner, H. Connectivity as a Crucial Determinant of Badland Morphology and Evolution. *Geomorphology* **2008**, *100*, 91–103. [CrossRef]
13. Fryirs, K. (Dis)Connectivity in Catchment Sediment Cascades: A Fresh Look at the Sediment Delivery Problem. *Earth Surf. Process. Landf.* **2013**, *38*, 30–46. [CrossRef]
14. Heckmann, T.; Schwanghart, W. Geomorphic Coupling and Sediment Connectivity in an Alpine Catchment—Exploring Sediment Cascades Using Graph Theory. *Geomorphology* **2013**, *182*, 89–103. [CrossRef]
15. Poeppl, R.E.; Parsons, A.J. The Geomorphic Cell: A Basis for Studying Connectivity. *Earth Surf. Process. Landf.* **2018**, *43*, 1155–1159. [CrossRef]
16. Borselli, L.; Cassi, P.; Torri, D. Prolegomena to Sediment and Flow Connectivity in the Landscape: A GIS and Field Numerical Assessment. *CATENA* **2008**, *75*, 268–277. [CrossRef]
17. Cavalli, M.; Trevisani, S.; Comiti, F.; Marchi, L. Geomorphometric Assessment of Spatial Sediment Connectivity in Small Alpine Catchments. *Geomorphology* **2013**, *188*, 31–41. [CrossRef]
18. Chartin, C.; Evrard, O.; Laceby, J.P.; Onda, Y.; Ottlé, C.; Lefèvre, I.; Cerdan, O. The Impact of Typhoons on Sediment Connectivity: Lessons Learnt from Contaminated Coastal Catchments of the Fukushima Prefecture (Japan): Typhoon Impact on Sediment Connectivity–Fukushima, Japan. *Earth Surf. Process. Landf.* **2017**, *42*, 306–317. [CrossRef]
19. Ali, G.; Oswald, C.; Spence, C.; Wellen, C. The T-TEL Method for Assessing Water, Sediment, and Chemical Connectivity. *Water Resour. Res.* **2018**, *54*, 634–662. [CrossRef]

20. Baartman, J.E.M.; Masselink, R.; Keesstra, S.D.; Temme, A.J.A.M. Linking Landscape Morphological Complexity and Sediment Connectivity. *Earth Surf. Process. Landf.* **2013**, *38*, 1457–1471. [CrossRef]
21. Coulthard, T.J.; Van De Wiel, M.J. Modelling Long Term Basin Scale Sediment Connectivity, Driven by Spatial Land Use Changes. *Geomorphology* **2017**, *277*, 265–281. [CrossRef]
22. Kondolf, G.M.; Boulton, A.J.; O'Daniel, S.; Poole, G.C.; Rahel, F.J.; Stanley, E.H.; Wohl, E.; Bång, A.; Carlstrom, J.; Cristoni, C.; et al. Process-Based Ecological River Restoration: Visualizing Three-Dimensional Connectivity and Dynamic Vectors to Recover Lost Linkages. *Ecol. Soc.* **2006**, *11*, 13–37. [CrossRef]
23. Poeppl, R.E.; Keesstra, S.D.; Maroulis, J. A Conceptual Connectivity Framework for Understanding Geomorphic Change in Human-Impacted Fluvial Systems. *Geomorphology* **2017**, *277*, 237–250. [CrossRef]
24. Cavalli, M.; Vericat, D.; Pereira, P. Mapping Water and Sediment Connectivity. *Sci. Total Environ.* **2019**, *673*, 763–767. [CrossRef] [PubMed]
25. Grauso, S.; Pasanisi, F.; Tebano, C. Assessment of a Simplified Connectivity Index and Specific Sediment Potential in River Basins by Means of Geomorphometric Tools. *Geosciences* **2018**, *8*, 48. [CrossRef]
26. Ludwig, J.A.; Bastin, G.N.; Chewings, V.H.; Eager, R.W.; Liedloff, A.C. Leakiness: A New Index for Monitoring the Health of Arid and Semiarid Landscapes Using Remotely Sensed Vegetation Cover and Elevation Data. *Ecol. Indic.* **2007**, *7*, 442–454. [CrossRef]
27. Capolongo, D.; Refice, A.; Bocchiola, D.; D'Addabbo, A.; Vouvalidis, K.; Soncini, A.; Zingaro, M.; Bovenga, F.; Stamatopoulos, L. Coupling Multitemporal Remote Sensing with Geomorphology and Hydrological Modeling for Post Flood Recovery in the Strymonas Dammed River Basin (Greece). *Sci. Total Environ.* **2019**, *651*, 1958–1968. [CrossRef] [PubMed]
28. Cantreul, V.; Bielders, C.; Calsamiglia, A.; Degré, A. How Pixel Size Affects a Sediment Connectivity Index in Central Belgium. *Earth Surf. Process. Landf.* **2018**, *43*, 884–893. [CrossRef]
29. Fuller, I.C.; Large, A.R.G.; Charlton, M.E.; Heritage, G.L.; Milan, D.J. Reach-Scale Sediment Transfers: An Evaluation of Two Morphological Budgeting Approaches. *Earth Surf. Process. Landf.* **2003**, *28*, 889–903. [CrossRef]
30. Poole, G.C.; Stanford, J.A.; Running, S.W.; Frissell, C.A. Multiscale Geomorphic Drivers of Groundwater Flow Paths: Subsurface Hydrologic Dynamics and Hyporheic Habitat Diversity. *J. N. Am. Benthol. Soc.* **2006**, *25*, 288–303. [CrossRef]
31. Sidle, R.C.; Gomi, T.; Loaiza Usuga, J.C.; Jarihani, B. Hydrogeomorphic Processes and Scaling Issues in the Continuum from Soil Pedons to Catchments. *Earth-Sci. Rev.* **2017**, *175*, 75–96. [CrossRef]
32. Cavalli, M.; Tarolli, P.; Dalla Fontana, G.; Marchi, L. Multi-Temporal Analysis of Sediment Source Areas and Sediment Connectivity in the Rio Cordon Catchment (Dolomites). *Rendiconti Online Della Soc. Geol. Ital.* **2016**, *39*, 27–30. [CrossRef]
33. de Musso, N.M.; Capolongo, D.; Caldara, M.; Surian, N.; Pennetta, L. Channel Changes and Controlling Factors over the Past 150 Years in the Basento River (Southern Italy). *Water* **2020**, *12*, 307. [CrossRef]
34. Kalantari, Z.; Cavalli, M.; Cantone, C.; Crema, S.; Destouni, G. Flood Probability Quantification for Road Infrastructure: Data-Driven Spatial-Statistical Approach and Case Study Applications. *Sci. Total Environ.* **2017**, *581–582*, 386–398. [CrossRef] [PubMed]
35. Kuo, C.-W.; Brierley, G. The Influence of Landscape Connectivity and Landslide Dynamics upon Channel Adjustments and Sediment Flux in the Liwu Basin, Taiwan. *Earth Surf. Process. Landf.* **2014**, *39*, 2038–2055. [CrossRef]
36. Lisenby, P.E.; Fryirs, K.A.; Thompson, C.J. River Sensitivity and Sediment Connectivity as Tools for Assessing Future Geomorphic Channel Behavior. *Int. J. River Basin Manag.* **2019**, 1–48. [CrossRef]
37. Rinaldi, M.; Amponsah, W.; Benvenuti, M.; Borga, M.; Comiti, F.; Lucía, A.; Marchi, L.; Nardi, L.; Righini, M.; Surian, N. An Integrated Approach for Investigating Geomorphic Response to Extreme Events: Methodological Framework and Application to the October 2011 Flood in the Magra River Catchment, Italy. *Earth Surf. Process. Landf.* **2016**, *41*, 835–846. [CrossRef]
38. Surian, N.; Righini, M.; Lucía, A.; Nardi, L.; Amponsah, W.; Benvenuti, M.; Borga, M.; Cavalli, M.; Comiti, F.; Marchi, L.; et al. Channel Response to Extreme Floods: Insights on Controlling Factors from Six Mountain Rivers in Northern Apennines, Italy. *Geomorphology* **2016**, *272*, 78–91. [CrossRef]
39. Arnaud-Fassetta, G.; Astrade, L.; Bardou, É.; Corbonnois, J.; Delahaye, D.; Fort, M.; Gautier, E.; Jacob, N.; Peiry, J.-L.; Piégay, H.; et al. Fluvial geomorphology and flood-risk management. *Géomorphologie Relief Process. Environ.* **2009**, *15*, 109–128. [CrossRef]

40. Zingaro, M.; Refice, A.; Giachetta, E.; D'Addabbo, A.; Lovergine, F.; De Pasquale, V.; Pepe, G.; Brandolini, P.; Cevasco, A.; Capolongo, D. Sediment Mobility and Connectivity in a Catchment: A New Mapping Approach. *Sci. Total Environ.* **2019**, *672*, 763–775. [CrossRef]
41. Messenzehl, K.; Hoffmann, T.; Dikau, R. Sediment Connectivity in the High-Alpine Valley of Val Müschauns, Swiss National Park—Linking Geomorphic Field Mapping with Geomorphometric Modelling. *Geomorphology* **2014**, *221*, 215–229. [CrossRef]
42. Schneevoigt, N.J.; van der Linden, S.; Thamm, H.-P.; Schrott, L. Detecting Alpine Landforms from Remotely Sensed Imagery. A Pilot Study in the Bavarian Alps. *Geomorphology* **2008**, *93*, 104–119. [CrossRef]
43. Walling, D.E.; Zhang, Y. Predicting Slope-Channel Connectivity: A National-Scale Approach. In *Sediment Transfer through the Fluvial System, Proceedings of a symposium held in Moscow, 2–6 August 2004*; Golosov, V., Belyaev, V., Walling, D.E., Eds.; IAHS: Wallingford, UK, 2004; No. 288; pp. 107–114.
44. Duong Thi, T.; Do Minh, D. Riverbank Stability Assessment under River Water Level Changes and Hydraulic Erosion. *Water* **2019**, *11*, 2598. [CrossRef]
45. Zanetti, C.; Macia, J.; Liency, N.; Vennetier, M.; Mériaux, P.; Provansal, M. Roles of the Riparian Vegetation: The Antagonism between Flooding Risk and the Protection of Environments. *E3S Web Conf.* **2016**, *7*, 13015. [CrossRef]
46. Zischg, A.P.; Galatioto, N.; Deplazes, S.; Weingartner, R.; Mazzorana, B. Modelling Spatiotemporal Dynamics of Large Wood Recruitment, Transport, and Deposition at the River Reach Scale during Extreme Floods. *Water* **2018**, *10*, 1134. [CrossRef]
47. Gregory, K.J.; Thornes, J.B. The Severn Basin: Sample Basin Review [Le Bassin de La Severn]. *Quaternaire* **1980**, *17*, 61–64. [CrossRef]
48. Hillier, R.D.; Williams, B.P.J. The alluvial OLD Red Sandstone: Fluvial Basins. In *The Geology of England and Wales*; Brenchley, P.J., Rawson, P.F., Eds.; The Geological Society: London, UK, 2006; pp. 155–172.
49. Maddy, D.; Green, C.P.; Lewis, S.G.; Bowen, D.Q. Pleistocene Geology of the Lower Severn Valley, U.K. *Quat. Sci. Rev.* **1995**, *14*, 209–222. [CrossRef]
50. Hooke, J.; Sandercock, P.; Cammeraat, L.H.; Lesschen, J.P.; Borselli, L.; Torri, D.; Meerkerk, A.; van Wesemael, B.; Marchamalo, M.; Barbera, G.; et al. Mechanisms of Degradation and Identification of Connectivity and Erosion Hotspots. In *Combating Desertification and Land Degradation*; Springer: Cham, Switzerland, 2017; pp. 13–37. [CrossRef]
51. Lizaga, I.; Quijano, L.; Palazón, L.; Gaspar, L.; Navas, A. Enhancing Connectivity Index to Assess the Effects of Land Use Changes in a Mediterranean Catchment. *Land Degrad. Dev.* **2018**, *29*, 663–675. [CrossRef]
52. Wohl, E.; Rathburn, S.; Chignell, S.; Garrett, K.; Laurel, D.; Livers, B.; Patton, A.; Records, R.; Richards, M.; Schook, D.M.; et al. Mapping Longitudinal Stream Connectivity in the North St. Vrain Creek Watershed of Colorado. *Geomorphology* **2017**, *277*, 171–181. [CrossRef]
53. Tanguy, M.; Dixon, H.; Prosdocimi, I.; Morris, D.G.; Keller, V.D.J. Gridded Estimates of Daily and Monthly Areal Rainfall for the United Kingdom (1890–2015) [CEH-GEAR]. Available online: https://doi.org/10.5285/33604EA0-C238-4488-813D-0AD9AB7C51CA (accessed on 26 June 2020).
54. Keller, V.D.J.; Tanguy, M.; Prosdocimi, I.; Terry, J.A.; Hitt, O.; Cole, S.J.; Fry, M.; Morris, D.G.; Dixon, H. CEH-GEAR: 1 Km Resolution Daily and Monthly Areal Rainfall Estimates for the UK for Hydrological and Other Applications. *Earth Syst. Sci. Data* **2015**, *7*, 143–155. [CrossRef]
55. Cevasco, A.; Pepe, G.; Brandolini, P. The Influences of Geological and Land Use Settings on Shallow Landslides Triggered by an Intense Rainfall Event in a Coastal Terraced Environment. *Bull. Eng. Geol. Environ.* **2014**, *73*, 859–875. [CrossRef]
56. Wilson, M.F.J.; O'Connell, B.; Brown, C.; Guinan, J.C.; Grehan, A.J. Multiscale Terrain Analysis of Multibeam Bathymetry Data for Habitat Mapping on the Continental Slope. *Mar. Geod.* **2007**, *30*, 3–35. [CrossRef]
57. Chini, M.; Hostache, R.; Giustarini, L.; Matgen, P. A Hierarchical Split-Based Approach for Parametric Thresholding of SAR Images: Flood Inundation as a Test Case. *IEEE Trans. Geosci. Remote Sens.* **2017**, *55*, 6975–6988. [CrossRef]
58. Giustarini, L.; Hostache, R.; Matgen, P.; Schumann, G.J.-P.; Bates, P.D.; Mason, D.C. A Change Detection Approach to Flood Mapping in Urban Areas Using TerraSAR-X. *IEEE Trans. Geosci. Remote Sens.* **2013**, *51*, 2417–2430. [CrossRef]

59. Giustarini, L.; Vernieuwe, H.; Verwaeren, J.; Chini, M.; Hostache, R.; Matgen, P.; Verhoest, N.E.C.; De Baets, B. Accounting for Image Uncertainty in SAR-Based Flood Mapping. *Int. J. Appl. Earth Obs. Geoinformation* **2015**, *34*, 70–77. [CrossRef]
60. Giustarini, L.; Hostache, R.; Kavetski, D.; Chini, M.; Corato, G.; Schlaffer, S.; Matgen, P. Probabilistic Flood Mapping Using Synthetic Aperture Radar Data. *IEEE Trans. Geosci. Remote Sens.* **2016**, *54*, 6958–6969. [CrossRef]
61. Hostache, R.; Matgen, P.; Wagner, W. Change Detection Approaches for Flood Extent Mapping: How to Select the Most Adequate Reference Image from Online Archives? *Int. J. Appl. Earth Obs. Geoinformation* **2012**, *19*, 205–213. [CrossRef]
62. Matgen, P.; Hostache, R.; Schumann, G.; Pfister, L.; Hoffmann, L.; Savenije, H.H.G. Towards an Automated SAR-Based Flood Monitoring System: Lessons Learned from Two Case Studies. *Phys. Chem. Earth Parts ABC* **2011**, *36*, 241–252. [CrossRef]
63. Hostache, R.; Chini, M.; Giustarini, L.; Neal, J.; Kavetski, D.; Wood, M.; Corato, G.; Pelich, R.-M.; Matgen, P. Near-Real-Time Assimilation of SAR-Derived Flood Maps for Improving Flood Forecasts. *Water Resour. Res.* **2018**, *54*, 5516–5535. [CrossRef]
64. Wood, M.; Hostache, R.; Neal, J.; Wagener, T.; Giustarini, L.; Chini, M.; Corato, G.; Matgen, P.; Bates, P. Calibration of Channel Depth and Friction Parameters in the LISFLOOD-FP Hydraulic Model Using Medium-Resolution SAR Data and Identifiability Techniques. *Hydrol. Earth Syst. Sci.* **2016**, *20*, 4983–4997. [CrossRef]
65. Hostache, R.; Hissler, C.; Matgen, P.; Guignard, C.; Bates, P. Modelling Suspended-Sediment Propagation and Related Heavy Metal Contamination in Floodplains: A Parameter Sensitivity Analysis. *Hydrol. Earth Syst. Sci.* **2014**, *18*, 3539–3551. [CrossRef]
66. Lepesqueur, J.; Hostache, R.; Martínez-Carreras, N.; Montargès-Pelletier, E.; Hissler, C. Sediment Transport Modelling in Riverine Environments: On the Importance of Grain-Size Distribution, Sediment Density, and Suspended Sediment Concentrations at the Upstream Boundary. *Hydrol. Earth Syst. Sci.* **2019**, *23*, 3901–3915. [CrossRef]
67. Buraas, E.M.; Renshaw, C.E.; Magilligan, F.J.; Dade, W.B. Impact of Reach Geometry on Stream Channel Sensitivity to Extreme Floods. *Earth Surf. Process. Landf.* **2014**, *39*, 1778–1789. [CrossRef]
68. Comiti, F.; Lucía, A.; Rickenmann, D. Large Wood Recruitment and Transport during Large Floods: A Review. *Geomorphology* **2016**, *269*, 23–39. [CrossRef]
69. Krapesch, G.; Hauer, C.; Habersack, H. Scale Orientated Analysis of River Width Changes Due to Extreme Flood Hazards. *Nat. Hazards Earth Syst. Sci.* **2011**, *11*, 2137–2147. [CrossRef]
70. Sholtes, J.S.; Yochum, S.E.; Scott, J.A.; Bledsoe, B.P. Longitudinal Variability of Geomorphic Response to Floods: Geomorphic Response to Floods. *Earth Surf. Process. Landf.* **2018**, *43*, 3099–3113. [CrossRef]
71. Tamminga, A.D.; Eaton, B.C.; Hugenholtz, C.H. UAS-Based Remote Sensing of Fluvial Change Following an Extreme Flood Event. *Earth Surf. Process. Landf.* **2015**, *40*, 1464–1476. [CrossRef]